NUMERICAL STUDY OF HEAT TRANSFER IN A TURBULENT JET DISCHARGING INTO A CROSS-FLOW

Armando Alvarez de Souza, asouza@ita.br
Cláudia Regina de Andrade, claudia@ita.br
Edson Luiz Zaparoli, zaparoli@ita.br
Instituto Tecnológico de Aeronáutica – ITA, Departamento de Energia
Praça Mar. Eduardo Gomes, 50 – Vila das Acácias
São José dos Campos – SP CEP 12 228 900.

Abstract. Turbulent jets flows discharging into a crossflow are encountered in a variety of applications including pollutant discharges, drying of paper, textiles, combustion chamber design, film cooling of turbine blades and aircraft fluid discharges. The heat transfer and flow characteristics of the jet discharge into a crossflow are complex due to the inherent interactions becoming a good test to turbulence models. The main characteristics of the single jet discharging into a cross-flow are the formation of the counter-rotating bound vortex pair downstream from the jet exit, a horseshoe vortex system in the cross-flow boundary layer upstream from the jet exit, and the creation of wake vortices similar in appearance to those observed in the flow past a bluff body. This wake flow reattaches the jet emerging wall in a downstream distance depending on the jet to crossflow velocity ratio. In the present work, governing equations (mass conservation, momentum, energy and standard k-ε turbulence model) are discretized using a finite volume approach with a hexahedrical structured mesh to simulate this problem. The pressure and velocity fields are coupled employing the SIMPLE algorithm. Due to the importance for aeronautical applications, present numerical analysis is focused on the influence of the jet to crossflow velocity ratio on the temperature distribution along the reattachment region at the duct wall.

Keywords: cross-flow, turbulent jet, CVP, numerical simulation, heat transfer.

1. INTRODUCTION

The flow of turbulent jet discharge into a cross-flow are encountered in a variety of applications including pollutant discharges, VSTOL, combustion chamber design, and film cooling of turbine blades. These flows are difficult to predict accurately due to the inherent complexity of the jet-cross-flow interaction (Acharya et. al., 2000). The resultant flow shows a complex flow field with several distinct patterns, which includes; an embedded vortex pair along the path of the jet (CVP), complex system of vortices in the wake region and horseshoe vortices similar to the flow around a solid body attached to a wall, see Figure 1. The kidney-shaped vortex pair (CVP) formed by the cross flow shearing the jet and folding the downstream face over itself with increasing distance along the jet path, appears to be the major flow feature of a deflected jet. This counter rotating vortex pair (CVP) is always present over a wide range of Reynolds number and velocity ratio (Calay and Holdo, 1998). The vortex at the wake region appears to be periodic and unstable, however, the wake vortex are time-dependent phenomena. Such structure appears approximately with frequency of 0.098. The CVP and horseshoe vortex are steady and, however, they can be modeled with time-averaged models.

Several workers have studied numerically the jet in a cross-flow. In the 1980's, with the rapid advances in computational resources and with the development of better and faster algorithms, finite difference methods began to replace integral methods as the analysis tools of choice. Most numerical investigations of the jet in cross-flow after 1975 involved the solution of the Reynolds Averaged Navier Stokes (RANS) equations and the energy equation on a finite difference grid, with closure for turbulent quantities obtained through a turbulence model. The majority of the RANS simulations for jet in a cross flow have employed a variant of the k-ε model (originally proposed by Launder and Spalding, 1974) to obtain the distribution of eddy viscosity. Patankar et al. (1977) were among the early researchers to use this model to perform a detailed study of the jet in a cross flow, and even with a relatively coarse (15x15x10) grid, obtained reasonable agreement with experimental data for the jet trajectory and streamwise velocity.

Grid resolution requirements were investigated by Demuren (1983) in his computations for a row of jets in a cross-flow. Results for a 37x70x14 grid (stream wise, vertical and spanwise directions) were shown to be grid independent and captured experimental trends fairly well. Demuren (1983) also published a detailed analysis on modeling turbulent jets in cross flow, and presented a systematic review of the various models reported until 1985. Claus and Vanka (1990) used a refined grid (256x96x96) and the k-ε model and found that they could not capture the horseshoe vortex. Kim and Benson (1992) employed a multiple-time-scale turbulence model to perform a detailed analysis of the flowfield of a row of jets in a confined cross flow. The horseshoe structure was predicted correctly using a non-uniform 165x59x80 grid and the good agreement was attributed partly to the multiple-time-scale model used for this study. An analysis of cooling jets near the leading edge of turbine blades was performed by Benz et al. (1993). The RANS equations coupled with the standard k-ε model were solved using the SIMPLEC algorithm for compressible flows. Good agreement with experimental results was obtained due to the inclusion of the coolant delivery tube along with the main flow.

As seen so far, the issues of modeling errors in RANS and the non-universality of such turbulence models have rendered the use of such approximations unreliable in the case of complex turbulent flows (particularly for the cases for which the turbulence models are not calibrated). In DNS (Direct Numerical Simulation) approach, higher-order schemes have to be used, and all temporal and spatial scales are resolved; therefore, no modeling is required. Due to the resolution requirements, the computational effort required is severe, and since the resolution requirements increase with Re, DNS is limited to only low Re values.

In LES (Large Eddy Simulation) procedure, the large scales of the flows that are dependent on the boundary conditions and contain most of the kinetic energy of the flow are truly reproduced. The small scales or subgrid scales (SGS) are expected to be more universal and isotropic in nature, and these are modeled. Since only the large scales are resolved, resolution requirements are more modest, and high-Re LES calculations are feasible. To achieve decomposition in terms of resolved fields and subgrid fields, one generally applies a spatial filtering operation. Sharma and Acharya (1998) presented the direct numerical simulation of a rectangular coolant jet injected normally into a periodic cross-flow using high order spatial discretization on a 128×64×64 grid for a channel Reynolds number of 5600 and momentum ratio of 0.25. Jones and Willie (1996a, 1996b) presented the results using LES for a round and plane jets in cross-flow on an 87×30×30 mesh. The Reynolds number based on jet velocity and the nozzle width was 5,815, and the blowing ratio was 7.34.

In the present work the turbulent jet discharging in a cross-flow is numerically studied using a CFD tool. Governing equations (mass conservation, momentum and energy and standard k-ε turbulence model) are discretized using a finite volume approach with a hexahedral mesh to simulate this problem. Numerical results for the velocity magnitude are compared with experimental data presented in Calay and Holdo (1998) and showed good agreement related to flowfield patterns. The jet to cross-flow velocity ratios are tested for two heat transfer conditions: a cold jet discharging into a hot cross-flow and a hot jet discharging into a cold cross-flow. It is verified that for low velocity ratios (less than 1) the jet flow trajectory is strongly deflected by the cross-flow, occurring an interaction between the jet and cold bottom wall due to the undesirable jet reattachment.
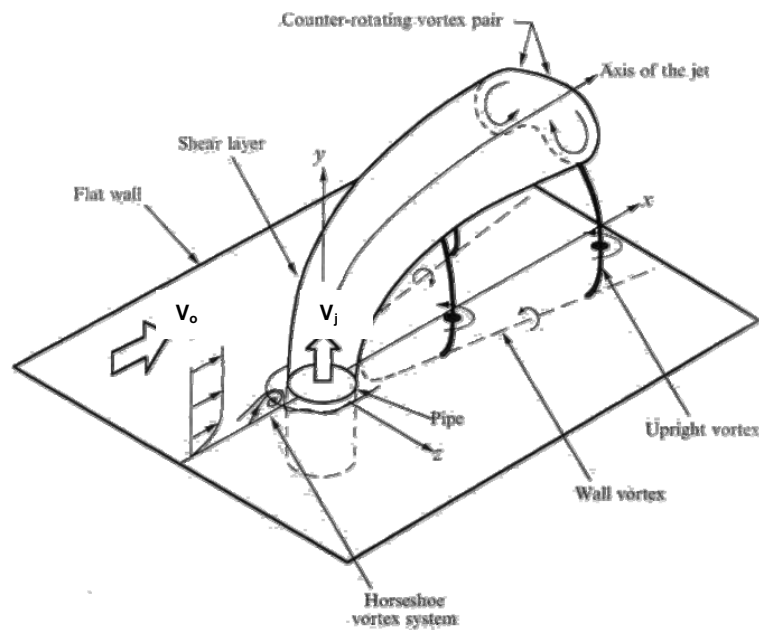
Figure 1 – Schematic of the flow field of a jet in cross-flow (adapted from Kelso and Perry, 1996)

2. MATHEMATICAL FORMULATION

The turbulent jet in cross-flow is studied under steady-state conditions with constant fluid thermophysical properties. The flow is assumed three-dimensional and incompressible. A schematic diagram of the geometry with dimensions and main boundary conditions is presented in Figure 2. The computational domain dimensions were performed similarly of the experimental set-up (Toften et al., 1993). RANS (Reynolds Average Navier-Stokes) and energy equations are employed to simulate thermal and turbulent flow fields. The turbulence effects are taken account employing an eddy viscosity based model (standard k-ε). So, the governing equations (mass conservation, momentum, energy, and turbulence model) are stated as:

$$\frac{\partial}{\partial x_i}(\rho \overline{u}_i) = 0 \tag{1}$$

$$\rho \overline{u}_j \frac{\partial \overline{u}_i}{\partial x_i} = -\frac{\partial \overline{p}}{\partial x_i} + \frac{\partial}{\partial x_j}\left[\mu_t\left(\frac{\partial \overline{u}_i}{\partial x_j} + \frac{\partial \overline{u}_j}{\partial x_i}\right)\right]; \quad \text{with } \mu_t = \rho C_\mu \frac{k^2}{\varepsilon} \tag{2}$$

$$\rho \overline{u}_j \frac{\partial \overline{T}}{\partial x_j} = \frac{\partial}{\partial x_j}\left[\left(\frac{\mu_L}{Pr} + \frac{\mu_t}{\sigma_T}\right)\frac{\partial \overline{T}}{\partial x_j}\right] \tag{3}$$

$$\rho \overline{u}_j \frac{\partial k}{\partial x_j} = \frac{\partial}{\partial x_j}\left(\frac{\mu_t}{\sigma_k}\frac{\partial k}{\partial x_j}\right) + \mu_t\left(\frac{\partial \overline{u}_i}{\partial x_j} + \frac{\partial \overline{u}_j}{\partial x_i}\right)\frac{\partial \overline{u}_i}{\partial x_j} - \rho \varepsilon \tag{4}$$

$$\rho \overline{u}_j \frac{\partial \varepsilon}{\partial x_j} = \frac{\partial}{\partial x_j}\left(\frac{\mu_t}{\sigma_\varepsilon}\frac{\partial k}{\partial x_j}\right) + C_1 \mu_t \frac{\varepsilon}{k}\left(\frac{\partial \overline{u}_i}{\partial x_j} + \frac{\partial \overline{u}_j}{\partial x_i}\right)\frac{\partial \overline{u}_i}{\partial x_j} - C_2 \rho \frac{\varepsilon^2}{k} \tag{5}$$

Where x_i are the Cartesian coordinates, and $\overline{u}_i$ are the corresponding velocity components; $\overline{T}$ = temperature field; k = turbulent kinetic energy; ε = turbulent energy dissipation rate; ρ = fluid density; μ_L = laminar viscosity; μ_t = turbulent viscosity; Pr = laminar Prandtl number. The constants that appear in the above equations are given by the following values: C_μ = 0.09, C_1 = 1.92, σ_k = 1.0, σ_ε = 1.3 and σ_T = 1.0.
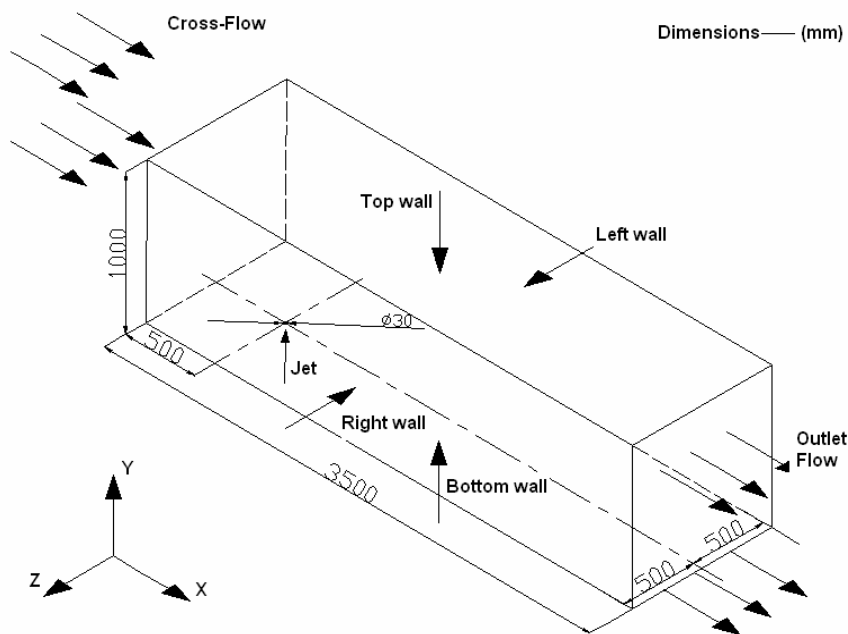
Figure 2a - Geometric domain and main boundary conditions
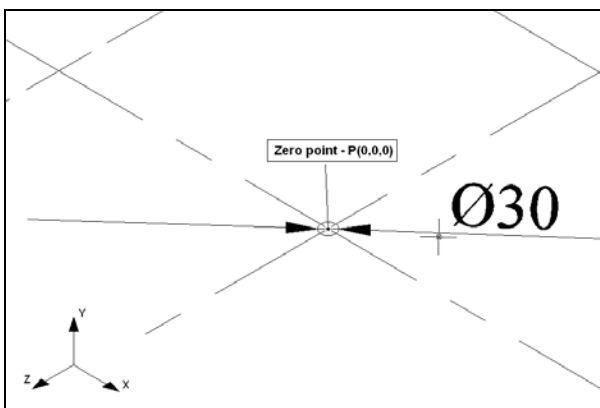
Figure 2b – Zoom around the jet exit
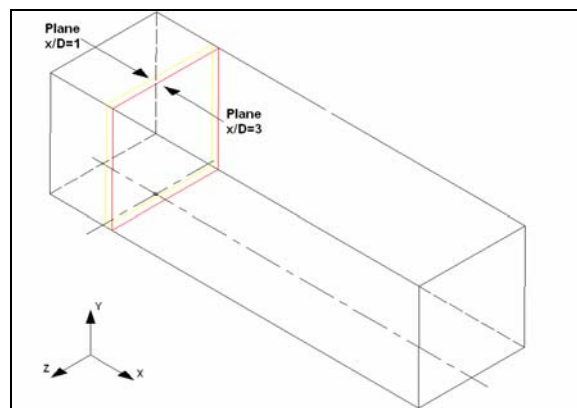
Figure 2c – Visualization of the planes

The Reynolds number is calculated based on the jet diameter (D) and its inlet velocity (V_j) with fluid density and dynamic viscosity of 1.225 kg/m^3 and 1.79·10^{-5} kg/m.s, respectively. Three different jet (V_j) to cross-flow (V_o) velocity ratios (R_v) were simulated (V_j/V_o = 0.5, 4 and 8) and two thermal conditions were prescribed: $R_t = T_j/T_o$ = 0.5 (cold jet discharging in hot cross-flow) and R_t = 2 (hot jet discharging in cold cross-flow). Turbulent quantities were specified using the data provided in Calay and Holdo (1998). Therefore, for all simulations, the cross-flow length scale and turbulence intensity were 50 mm and 4 %, respectively. For the jet flow, the viscosity ratio (μ_t /μ_L) and turbulence intensity were 30 and 1.5 %, respectively.

3. NUMERICAL SOLUTION

The CFD solution for the turbulent jet discharging into a cross-flow was divided in three steps, whose are: (i) pre-processor, (ii) solver and (iii) post-processor. The *pre-processing* consist in generation mesh and it was used GAMBIT to generate the geometric domain and mesh. In the second step (*solver*), the partial differential equations system given by Eq. (1) to (Eq. 5) is discretized and the resultant algebraic system is iteratively solved employing the FLUENT 6.3 package (a commercial CFD code based on the finite volume approach). This software has gradient adaptation tools, which allowed refining or coarsening our grid based on the flow solution parameters (Mach number, velocity, pressure, temperature). This procedure reduces strongly the total mesh cell number and insures a good quality solution, saving CPU processing time. The initial grid (without adaptive procedure and 173,000 cells) is illustrated in Figure 3a. Note the intense refinement required to capture the flow patterns around the jet exit (see also Figure 3b).
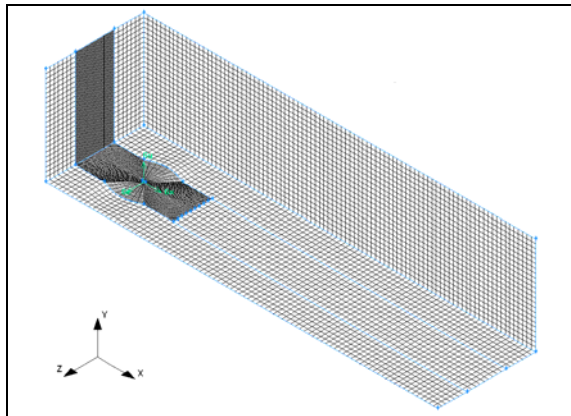
Figure 3a - Isometric view of the initial mesh generation procedure (173,000 cells)
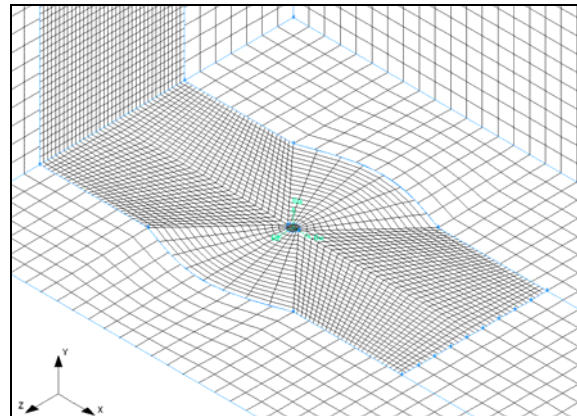
Figure 3b - Zoom around the jet exit

Figure 3b exhibits the final mesh (after adaptive procedure and 523,838 cells) on a longitudinal plane at jet centerline. The adaptive refinement is necessary to accomplish the jet spatial evolution, Fig. 4. Two intermediate meshes were also generated to evaluate if the mass balance is satisfactory. The centerline velocity profile at x/D = 1 was monitored during the solution, until the cells number contained in the mesh achieve a stabilized solution as can be observed in Figure 5 for five meshes. Note that the velocity profile plotted for 523,838 cells was identical to velocity profile obtained employing 750,000 cells. A mesh containing 523,838 cells provides us the same result and it doesn't need an excess refinement (higher computational cost). All graphics and results showed in this work are referent to the mesh with 523,838 cells and a comparison between the maximum velocity percent error at the plane x/D=1 to experimental data by Calay and Holdo (1998) is presented on Table 1.
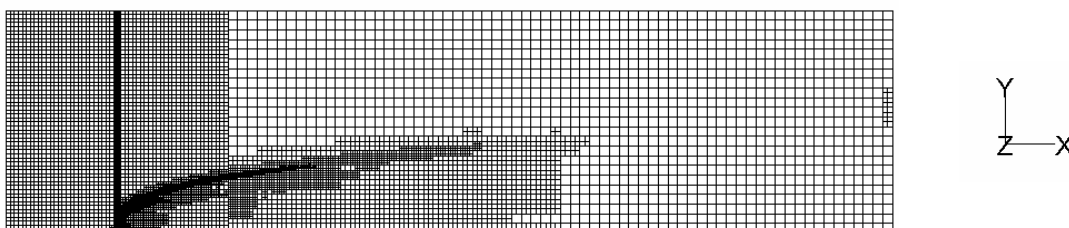
Figure 4 - Mesh on a longitudinal plane at jet centerline
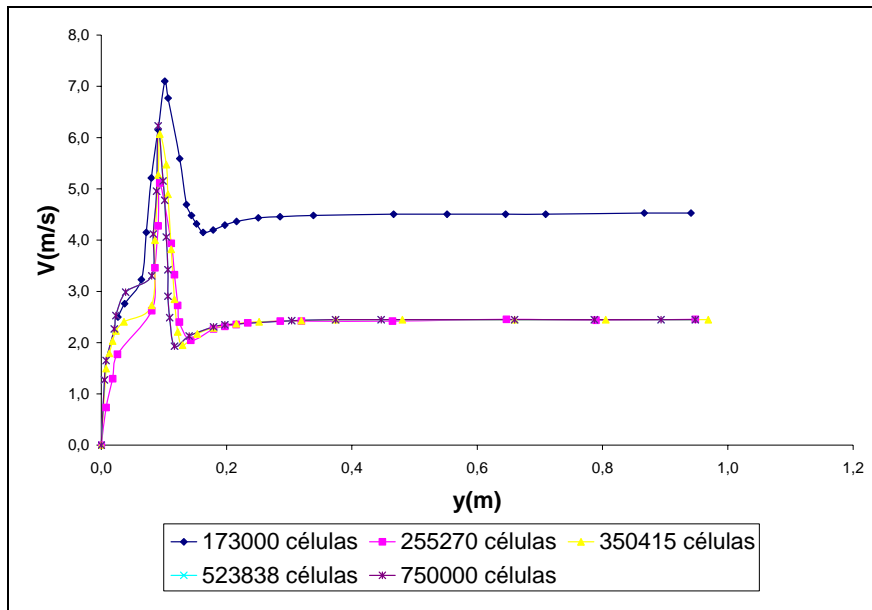
Figure 5 – Centerline velocity profile at x/D = 1 taken for mesh comparison

Table 1- Mass balance comparison as a function of the cell number

	Mesh 1	Mesh 2	Mesh 3	Mesh 4	Mesh 5
Cell number	173,000	255,269	350,413	523,838	523,838
Maximum velocity percent error at the plane x/D=1	13.50%	18.2%	12.5%	5.73%	5.73%

In the present work, the segregated algorithm (FLUENT, 2003) which allows each degree of freedom to be solved separately and sequentially, was selected for the iterative solution of the governing equations. Second-order discretization method was used to solve the transport equations because the flow is less diffusive and Calay and Holdo (1998) have gotten better agreement with experimental data using this second-order discretization method. First-order discretization method was used only in the beginning of the solution. The pressure and velocity fields are coupled employing the SIMPLE algorithm.

In the last step, the solution visualization is obtained using the FLUENT graphic interface. Variables (velocity components, pressure, temperature, turbulent quantities) contours and plots are available at pre-established user-defined planes.

4. RESULTS.

A comparison between numerical and experimental results (Calay e Holdo, 1998) for the velocity magnitude was carried out with the intent of achieving a reliable CFD solution. This validation case represents a three-dimensional circular jet (0.03 m diameter) discharging in a cross flow (see Fig. 2a). The jet to cross-flow velocity ratio ($R_v = V_j/V_o$) is equal to 4 and the boundary conditions are described in Table 2.

Table 2 - Inputs and boundary conditions for validation case.

$R_v = 4$	Boundary conditions	Velocity (m/s)
Cross-flow *(air)*	Velocity inlet	2.44
Jet *(air)*	Velocity inlet	9.76
Top wall *(solid)*	Wall	zero – No slip
Right wall *(solid)*	Wall	zero – No slip
Left wall *(solid)*	Wall	zero – No slip
Bottom wall *(solid)*	Wall	zero – No slip
Outlet flow *(air)*	Outflow	-------------

These velocity vector magnitude (V) profiles, along the spanwise direction, were non-dimensionalized by the cross-flow inlet velocity (V_o) and are plotted at x/D =1 and x/D = 3 positions, shown in Figure 6 and Figure 7, respectively.
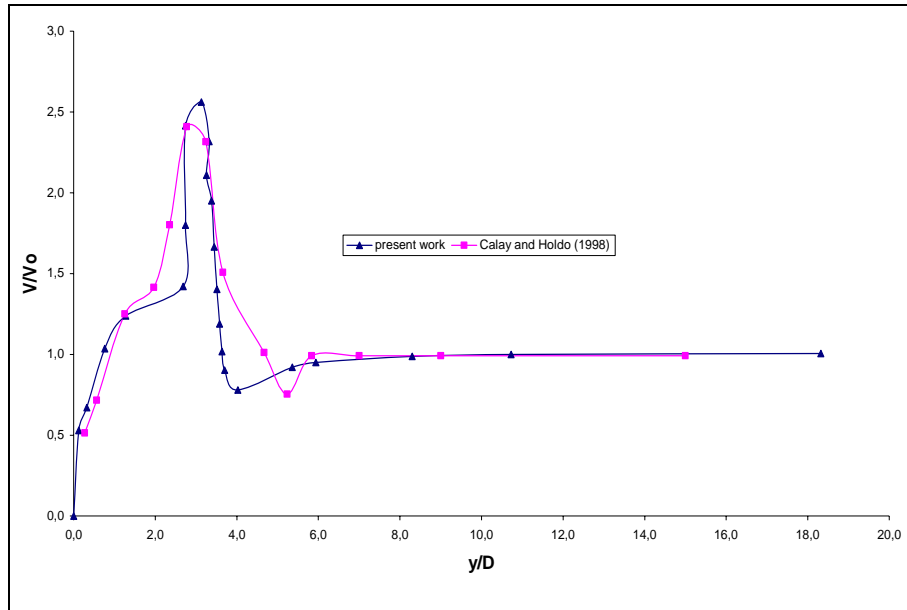
Figure 6 - Dimensionless velocity vector magnitude profile at x/D = 1 along the spanwise direction (y/D)

It is observed that the maximum centerline velocity values at x/D = 1 (see Figure 2c) was slightly overpredicted, but the percent error of 5.73% can be considered inside the experimental uncertainty interval. The maximum velocity point appeared at the position y/D=3.12 and presented a percent error of 12% in comparison with the experimental location. This difference can be probably attributed to the steady-state condition imposed to the simulation.
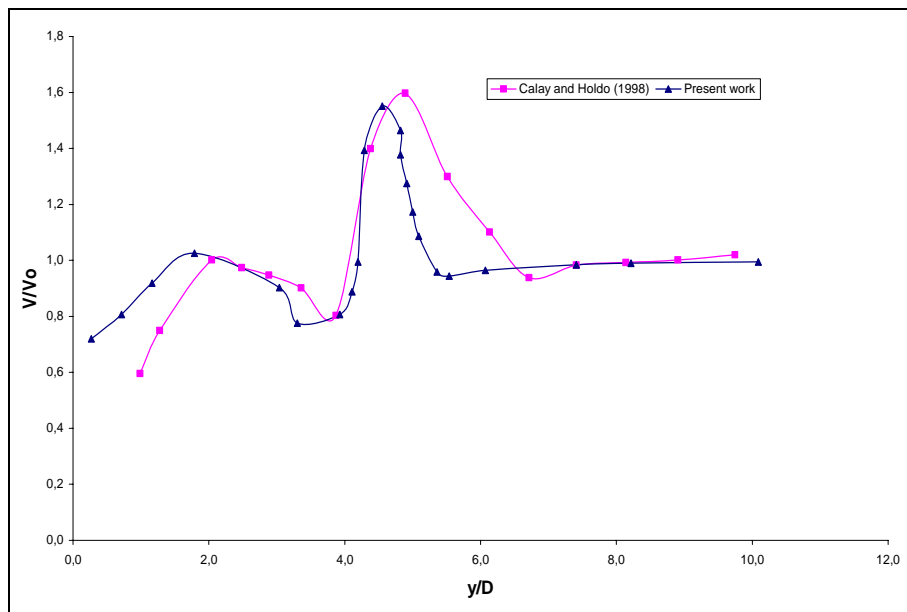
Figure 7 - Dimensionless velocity vector magnitude profile at x/D = 3 along the spanwise direction (y/D)

The maximum centerline velocity value at x/D = 3 (see Figure 2c) was slightly underpredicted because the percent error of 2.88% can be also considered inside the experimental uncertainty interval. The maximum velocity point appeared at y/D = 4.55 and it presented a percent error of 6.88%. As these results are in satisfactory agreement with experimental ones, the next step is to investigate the effect of the jet to cross-flow velocity and temperature ratio as detailed below.

4.1 Effect of the jet to cross-flow velocity and temperature ratio

Several simulations were performed to determine the jet in cross-flow structures and heat transfer characteristics. Velocity ratios of 0.5, 4 and 8 were used with two jet to cross-flow temperature ratios ($R_t = T_j/T_o$) as depicted in Table 3, Table 4 and Table 5, respectively. Boundary conditions and input values are also presented.

Table 3 - Inputs and boundary conditions for $R_v = 0.5$ with heat transfer conditions.

$R_v = 0.5$	Boundary conditions	Velocity (m/s)	Temperature (K) $R_t = 2$	Temperature (K) $R_t = 0.5$
Cross-flow (*air*)	Velocity	19.52	300	600
Jet (*air*)	Velocity	9.76	600	300
Top wall (*solid*)	Wall	zero – No slip	300	600
Right wall (*solid*)	Wall	zero – No slip	300	600
Left wall (*solid*)	Wall	zero – No slip	300	600
Bottom wall (*solid*)	Wall	zero – No slip	300	600
Outlet flow(*air*)	Outflow	-------------	-------------	-------------

Table 4 - Inputs and boundary conditions for $R_v = 4$ with heat transfer conditions.

$R_v = 4$	Boundary conditions	Velocity (m/s)	Temperature (K) $R_t = 2$	Temperature (K) $R_t = 0.5$
Cross-flow (*air*)	Velocity	2.44	300	600
Jet (*air*)	Velocity	9.76	600	300
Top wall (*solid*)	Wall	zero – No slip	300	600
Right wall (*solid*)	Wall	zero – No slip	300	600
Left wall (*solid*)	Wall	zero – No slip	300	600
Bottom wall (*solid*)	Wall	zero – No slip	300	600
Outlet flow(*air*)	Outflow	-------------	-------------	-------------

Table 5 - Inputs and boundary conditions for $R_v = 8$ with heat transfer conditions.

$R_v = 8$	Boundary conditions	Velocity (m/s)	Temperature (K) $R_t = 2$	Temperature (K) $R_t = 0.5$
Cross-flow (*air*)	Velocity	1.22	300	600
Jet (*air*)	Velocity	9.76	600	300
Top wall (*solid*)	Wall	zero – no slip	300	600
Right wall (*solid*)	Wall	zero – no slip	300	600
Left wall (*solid*)	Wall	zero – no slip	300	600
Bottom wall (*solid*)	Wall	zero – no slip	300	600
Outlet flow(*air*)	Outflow	-------------	-------------	-------------

As seen, the main parameter that affects the jet in a cross-flow is the velocity ratio. To observe the influence of the velocity ratio in the flow structure, it was plotted the jet trajectories along x and y-direction. Figure 8 shows the jet trajectory for the three velocity ratios presented before ($R_v = 0.5$; 4; 8). Note that, the jet trajectory is extremely deflected when the velocity ratio is decreased. When the velocity ratio was set up to 0.5, it appears a reverse flow region downstream the jet exit caused by the reattachment. The reattachment occurs due to lower velocity ratio, as can be seen in the dimensionless x-velocity contours traced in Fig. 9. Some particles of the jet return when they come upon to the reattachment. Figure 10 shows the particle pathline positioned at the point P (14, 0, 14), situated in the pipe exit, migrating towards the reattachment region. The particle has both negative and positive x-directions. Green, yellow and red colors represent positive x-velocities and light blue, light green and dark blue colors represent negative x-velocities. The reattachment region wasn't observed for both cases $R_v = 4$ and $R_v = 8$ due the high velocity ratio.
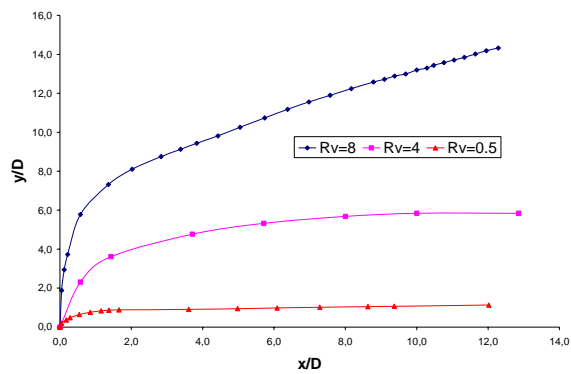
Figure 8 – Jet trajectories as a function the jet to cross-flow velocity ratio
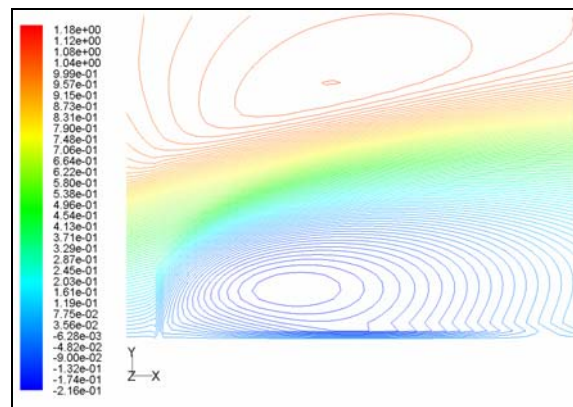
Figure 9 – Dimensionless x-velocity contours for $R_v = 0.5$
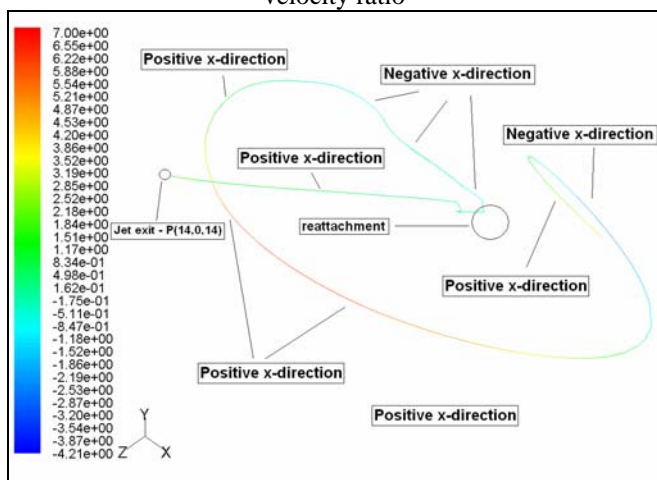
Figure 10 – Particle trajectory at point P(14,0,14)
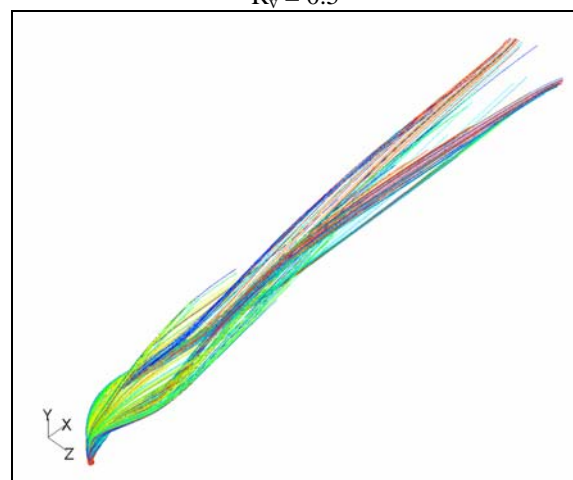
Figure 11 - Jet pathline for $R_v = 8$

Figure 11 presents the jet pathlines for $R_v = 8$ showing the jet trajectories roll-up causing the CVPs (Counter-rotating Vortex Pair) initial development. The cross-flow and jet interaction causes jet deflection and the cross-flow drag (suction) due to the jet stream momentum transfer. The intensity of these phenomena depends on the jet to cross-flow velocity ratios. At larger R_v values, the jet issues and pass over the cross-flow without deflection.

Figure 12 shows the dimensionless velocity contours for $R_v = 8$. Note that arise some vortices called "ring vortices". These vortices appear in the jet shear layer in both right and left sides. Ring vortices are detached of the jet shear layer and convected downstream, merging with CVPs structures.
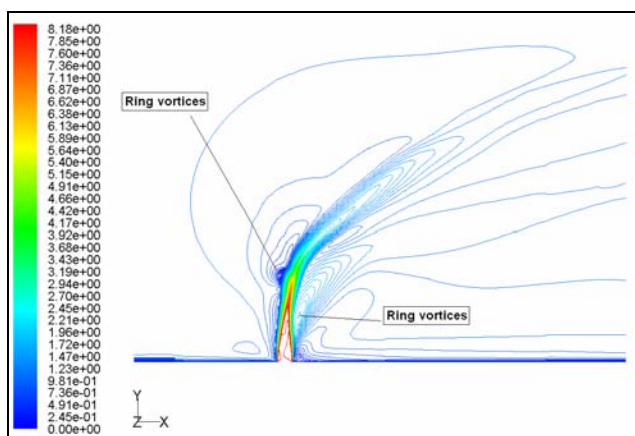
Figure 12 – Dimensionless velocity contours for $R_v = 8$
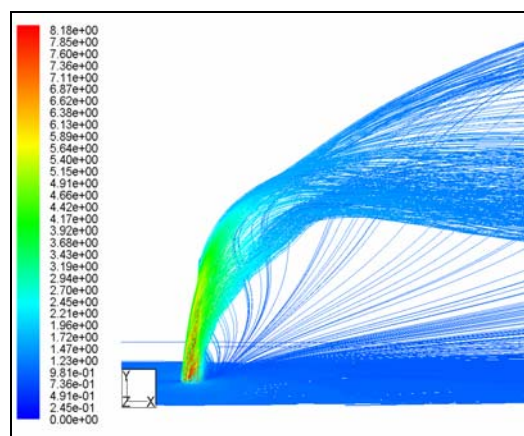
Figure 13 - Flow structure (pathlines) colored by velocity magnitude at the plane y/D = 0.66

Figure 13 illustrates particles pathlines at a plane y/D = 0.66 for visualization of the cross-flow drag phenomenon. It is observed that the cross-flow is suctioned by the jet displacement. When the jet is deflected by the cross-flow, an adverse pressure gradient region is generated. As a consequence, the boundary layer close to the jet and the cross-flow is lifted and merged with the jet along x-direction.

Figure 14 presents the dimensionless velocity magnitude contours for the jet to cross-flow velocity ratio equal to 8 at the y-z section and different x/D planes (Figure 2a). It is observed the development of the CVPs showing a vertical "kidney shape" structure that migrates along the x-direction. It is observed that the maximum velocity in the CVPs corners decreases in magnitude as the x/D distance increases, but its spatial distribution is enlarged (although the figures aren't obeying the same spatial scale). This effect is related with the mixing of the jet and cross-flow streams.

(a)

(b)

(c)

(d)
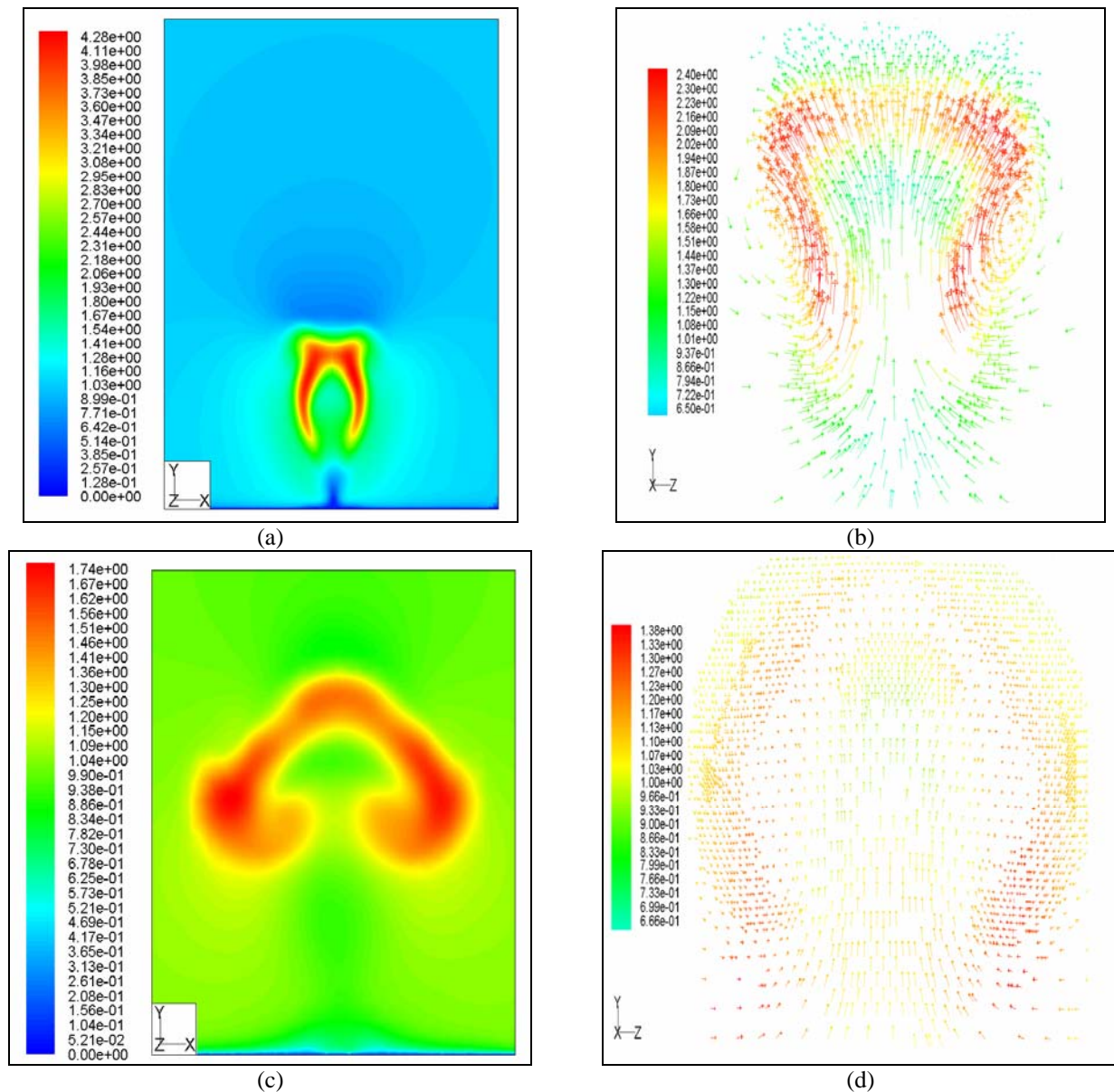
Figure 14 – Dimensionless velocity magnitude at the y-z plane for different x/D distances - evolution of CVPs.

To compare the two heat transfer conditions ($R_t = 0.5$ and $R_t = 2$), a dimensionless temperature was defined as:

$$\theta = \frac{T - T_0}{T_j - T_0}$$

(6)

Figure 15 shows the dimensionless temperature contours for the hot jet discharging in the cold cross-flow ($R_t = 2$) and the cold jet discharging in the hot cross-flow ($R_t = 0.5$), while the dimensionless temperature profiles at x/D = 1 along the spanwise direction (y/D) are plotted in Fig. 16.
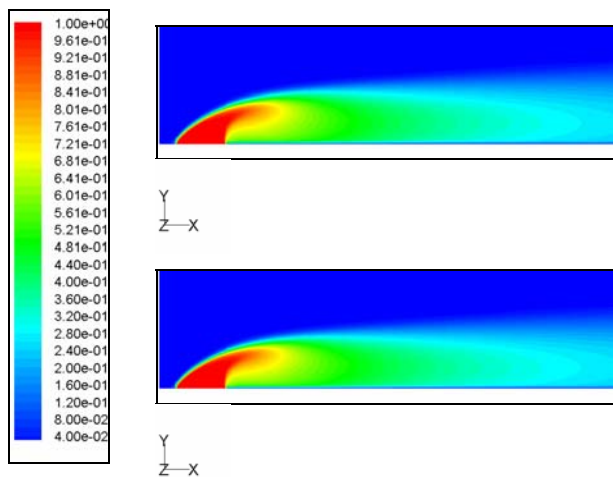
Figure 15 - Dimensionless temperature contours for (a) $R_t = 2$ e (b) $_t = 0.5$
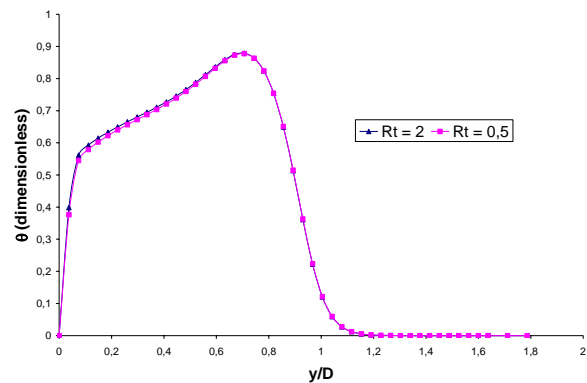
Figure 16 - Dimensionless temperature profiles at x/D = 1 along the spanwise direction (y/D).

Note that the dimensionless temperature contours for both cases $R_t = 2$ and $R_t = 0.5$ (Figs. 15a and 15b) are similar and aren't determined by the velocity and temperature fields interaction (as occurs in the natural convection, e.g.). Besides, this illustrates an incompressible fluid flow problem with heat transfer (employing a segregated method for solving). At compressible fluid flow regime or natural convection problems, a coupled numerical scheme is recommended.

5. CONCLUSIONS

In the present work, the turbulent jet flow discharging in a cross-flow was numerically studied. Experimental and numerical solution obtained for different jet to cross-flow velocity ratios (V_j/V_o) showed good agreement. The CVPs structures and reattachment regions were well captured showing that the V_j/V_o parameter is a determining factor in the flow structures development. A reliable CFD tool simulation of these flow and heat transfer characteristics (reattachment point, e.g.) is extremely important, especially in aeronautical applications. At this case, the reattachment region can define if the aircraft fuselage surface could be affected by the cabin compressible air discharge (focus of future works).

6. REFERENCES

Acharya, S., Tyagi, M. and Hoda A., 2000, "Flow and Heat Transfer Predictions for Film Cooling", Mechanical Engineering Department, Louisiana State University, Baton Rouge, LA 70803.

Calay, R.K. and Holdo, A.E., 1998, "Free-stream turbulence effects on a jet in a cross-flow", University of Hertfordshire, Hatfield, Herts, AL10-9AB, England.

Launder, B., E., and Spalding, D., B., 1974, Comp. Methods Appl. Mech. Eng., vol. 3, pp. 269.

Patankar, S. V., Basu, D. K., and Alpay, S. A., 1977, J. Fluids Engng., vol. 99, no. 4, pp. 758-762.

Demuren, A. O., 1983, Comp. Meth. App. Mech. Engr., vol. 37, pp. 309-328.

Claus, R. W. and Vanka, S. P., 1990, AIAA Paper No. 90-0444.

Kim, S. W., and Benson, T. J., 1993, AIAA Journal, Vol. 31, No. 5, pp. 806-811

Benz, E., Wittig, S., Beeck, A., and Fottner, L., 1993, AGARD-CP-534.

Sharma, C. and Acharya, S., 1998, NASA/CR-1998-208674.

Jones, W. P. and Wille, M., 1996a, Engineering Turbulence Modeling and Experiments 3. Ed. Rodi, W. and Bergeles, G. pp.199-209.

Jones, W. P. and Wille, M., 1996b, Int. J. Heat and Fluid Flow, Vol. 17, pp.296-306.

Toften T.H., Holds A.E and Kapfer D., 1993, "Effects of free-stream turbulence on a jet in a cross flow", In AGARD Conference Proceedings 534, Computational and Experimental Assessment of Jet in Cross Flow, France.